Voids and Yolk−Shells from Crystals That Coat Particles

Melinda Sindoro[†] and Steve Granick*,[†,‡,§]

[†]Department of Chemistry, [‡]Department of Materials Science and Engineering, and [§]Department of Physics, University of Illinois, Urbana, Illinois 61801, United States

S *Supporting Information*

ABSTRACT: We investigate curvature-driven core−shell morphology that emerges when polycrystalline shells of ZIF-8 (zeolitic imidazolate framework coordination polymer) grow on colloid-sized particles. In early growth stages, the shell is continuous, but it transforms to yolk−shell, with neither sacrificial template nor core etching, because of geometrical frustration. A design rule is developed regarding how local surface curvature matters. Comparing shells grown on cubic, rod-like, and peanut-shaped hematite core particles, we validate the argument.

This paper shows that surface curvature can be used to generate interfacial strain in growing yolk−shell structures, allowing one to design core−shell morphology. Here, the shells are porous coordination polymer and the strain arises from lattice mismatch during crystal growth. Unlike earlier examples of yolk−shell formation from porous coordination polymers,[1,2] sacrificial templates are not required. The arguments presented here about curvature-induced frustrated crystal growth, on which this study is based, are validated qualitatively by comparing growth on cubic, rod-like, and peanut-shaped core particles. The fascinating yolk−shell structures may potentially be useful for selective catalysis,[1−3] drug delivery,[4,5] contrast agent,[6] and sensing.[7]

Our shells are produced by wet chemistry, but the consequences for interfacial strain resemble those for vacuum-grown thin films.[8] Our hypothesis is that the underlying geometric curvature, κ, should guide the direction of strain, and hence of stress, in the growing polycrystalline shell. When this is the case, a yolk−shell might result, defined by the shape of the core. In the context of the porous coordination polymers with which we work, matched cell parameters between the core and shell materials result in connected pores at the boundary of crystal growth,[9,10] while nonepitaxy encourages either incorporation of defects into the crystal[11,12] or amorphous core−shell growth.[13,14] In the latter case, this shell crystallinity depends on the adsorption−desorption equilibrium, which is a function of solubility,[15] and time to accomplish mass transport,[16] which is a function of shell material. Hence, we expect crystal regrowth from Ostwald ripening[17] at suitably long incubation times. From this principle, we aim to form voids. This idea, we test using a prototypical porous coordination polymer, zeolitic imidazolate frameworks 8 (ZIF-8). As the core, we first selected hematite, a crystal, for ease of optical imaging and its distinctive X-ray diffraction (XRD) signals.

We find that the adsorption of poly(vinylpyrrolidone) (PVP; M_w = 40 000 g/mol) facilitates the growth of ZIF-8 shells on various types of cores, from crystalline hematite to amorphous silica, while the resulting morphology (Figure S1) is the same regardless of whether one does this. Still, PVP presence is useful to promote the adsorption of Zn ions[18] and to minimize particle aggregation. In brief, first the core and PVP are incubated in methanol. The free polymer is then removed, as if present, it would promote undesirable free-standing ZIF-8 crystals. Then, the ZIF-8 precursors, $Zn(NO_3)_2 \cdot 6H_2O$ and 2-methylimidazole ligand in methanol, are added to initiate shell formation at room temperature. The morphology and crystal structure of the shells are characterized at different times to investigate the growth mechanism.

There are several features immediately obvious upon imaging with TEM the yolk−shell formation pathway (Figure 1b−d):
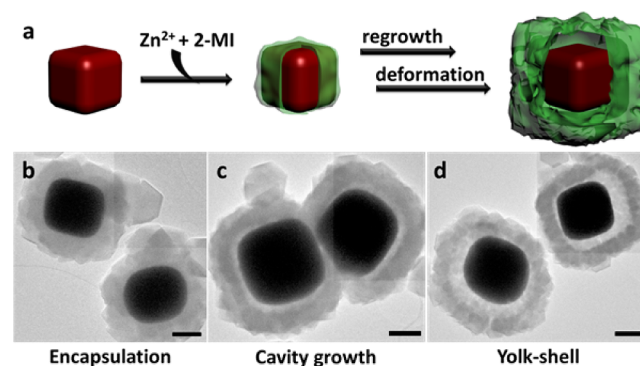

Figure 1. (a) Schematic concept of yolk−shell formation with cubic hematite crystal as the core. To illustrate this, transmission electron microscope (TEM) images of the growth pathway were taken at: (b) 6 h (encapsulation), (c) 24 h (cavity growth), and (d) 72 h (yolk−shell). Scale bars: 500 nm.

(1) the shell nucleates directly on the core particles, creating polycrystalline continuous coverage; (2) the cavity between the core and the shell builds over time; and (3) the same average shell thickness persists from the initial encapsulation to the final yolk−shell stage. Similarly, surface investigation using scanning electron microscopy (SEM) shows that the shell conforms to the shape of the core particles. At the encapsulation stage (Figure 2c,d) of low crystallinity, the surface topography is less defined, while the cubic morphology is more pronounced after the formation of cavity at the yolk−shell stage (Figure 2f,g).
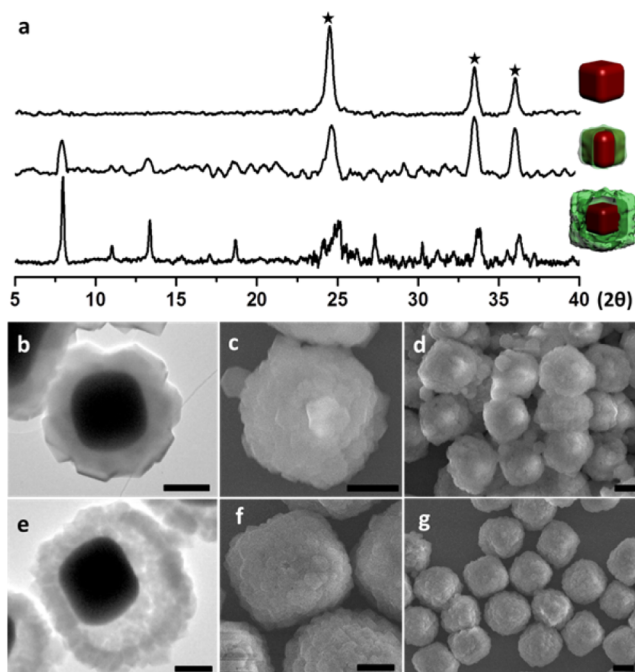
Figure 2. (a) XRD of (top) cubic hematite crystals, (middle) encapsulated hematite@ZIF-8, and (bottom) yolk−shell hematite@ZIF-8. Encapsulated hematite@ZIF-8 imaged by TEM (b) and SEM (c and d). Yolk−shell of hematite@ZIF-8 imaged by TEM (e) and SEM (f and g). Scale bars: 500 nm.

Notice that the shell exhibits no pattern of packing. The polycrystalline domains appear to coat the surface randomly.

The crystallinity of the shell was monitored by XRD during its growth. Considering the known kinetic formation of free-standing ZIF-8 in methanol in the first 24 h,[18,19] we expected the crystals to nucleate after a few hours, and indeed, the time range for free-standing crystal growth is the same as for cavity formation of the yolk−shell (∼24 h). Nonoverlapping XRD peaks obtained from the core cubic hematite (Figure 2a, top) are marked (★) for comparison at 2θ = 24.4, 34.3, and 35.9. Figure 2e shows that partial crystallinity, indicated by minor peaks at 2θ = 7.9 and 13.4, is observed for ZIF-8 shell at the encapsulation stage (<8 h). In contrast, prominent ZIF-8 peaks are obtained for the final yolk−shell structure. They agree with the known peaks of simulated ZIF-8 powders. This is additional evidence, beyond the TEM and SEM images, for the lack of oriented growth in the shell.

Notice that ZIF-8 recrystallization is necessary to form yolk−shell; this cavity formation mechanism requires reversible exchange of metal and ligand precursors from excess concentration in liquid to solid. Under conditions where we denied the excess of metal and ligand precursor needed to produce additional crystal growth, the intermediate structure was effectively arrested. We simulated deficiency of the precursor concentration by exchanging the supernatant with pure methanol, and found that the various growth stages formed at different elapsed time were stable, whether dispersed in pure solvent or vacuum-dried (Figure S2). While it is true that excess precursor also promotes the nucleation of unwanted free-standing ZIF-8 crystals, they can be separated during purification as their density (ρ_{ZIF-8} = 1.45 g/mL) is less than that of the yolk−shell ($\rho_{hematite}$ = 5.3 g/mL), causing slower sedimentation when the mixture is suspended in glycerol (ρ = 1.26 g/mL). It is unsurprising that the size and the

crystallization rate of free-standing ZIF-8 is unaffected by the presence of core particles, considering that heterogeneous growth is confined to the particle surface. On the other hand, as shell growth and recrystallization on particles is slower than on free-standing ZIF-8 crystals, the resulting polycrystalline shells are comparatively smaller (Figure S3).

In this scheme, voids between shell and core are the expected outcome of shell polycrystallinity. Shell domains initiate at multiple nucleation points with similar growth rate. As this produces stress when crystalline domains crowd against one another, one might expect one pathway to release by outward growth, away from the core. However, the lattice symmetry of ZIF-8 is incompatible with anisotropic growth that is preferentially perpendicular to the core; crystal growth is equally likely in all directions.[20] As a result, the polycrystalline shell thickness is also limited by the crystal's capacity to grow parallel to the core surface.

This is how the allowed shapes depend on geometric curvature (κ). Figure 3 illustrates how all final yolk−shell
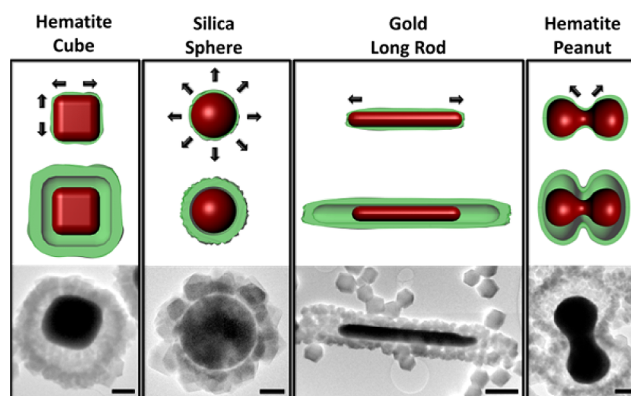

Figure 3. Schematic illustrations of the dominant deformation directions during shell growth (top) and while yolk−shell structures form (middle), accompanied by representative TEM images (bottom). Scale bars: 500 nm.

structures depend on various shapes of the core. A cubic hematite particle (6 planar surfaces: κ = 0) produces stress in the growing shell in all directions equally; hence, it shows a cavity that is large and symmetric. Spherical SiO_2 (convex surface: $\kappa > 0$) tolerates the growth of crystalline shell better; as a result, the cavity is fairly narrow. It is interesting that other particles possess both curvatures, planar and convex. For example, we found that long rods of Au (aspect ratio = 8) form cavities only at the tips, presumably owing to higher stress in the linear direction. Shorter rods of SiO_2 (aspect ratio = 2.5−3) produce yolk−shell structures with cavity preference along the linear direction too (Figure S5) but less well developed than when the rods are longer. To test the case of a concave surface ($\kappa < 0$), we synthesized peanut-shaped hematite, which is convex along the tips and concave along the waist. The convex geometry did not induce significant cavity formation, as expected by our hypothesis, but the coincidence of positive and negative curvatures forces stress to concentrate on the concave point. It is then alleviated by cavity development at the point where the curvature changes sign. This is confirmed by a close TEM look at the yolk−shell formation pathway of peanut-shaped hematite (Figure s6); cavity initiates from this spot.

Two additional points governing the formation of yolk−shell structures are first the balance between adsorption and

desorption rate of precursors on the growing crystals (in turn, it depends on external variables such as the solvent polarity, temperature, and precursor concentrations)[18] and, second, the density of nucleation points (this is because for a given precursor concentration, a large number of nucleation points yields smaller crystals and vice versa).[21] We find that this balance is easily tipped in two ways. To suppress nucleation sites, one can introduce a ligand modulator. To achieve this, we chose a molar equivalent of 1-methylimidazole. To augment the density of nucleation points, the concentration of metal and ligand precursors can be doubled. We found that small crystals (∼70 nm) mostly do not attach to the core particles or when they do, they do so at low surface coverage (Figure 4a). In
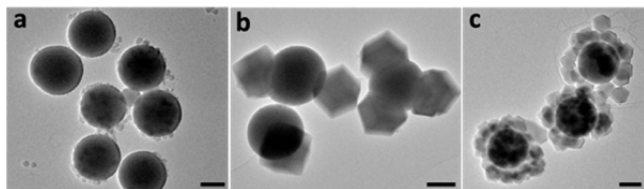

Figure 4. Influence of ZIF-8 crystal size. The core particles are spherical SiO_2. When crystals are too small (a) or too large (b), they attach poorly and continuous shells do not develop. To produce voids, the shell crystal must be in an intermediate sweet spot of size relative to the core particle. Scale bars: 500 nm.

contrast, large crystals (>850 nm) attach but fail to form a continuous shell (Figure 4b). This means that for a given crystal size, the size of the parent core particle dictates the number of shell nucleation points. This may explain why smaller nanoparticles are easily incorporated into crystal domains so that yolk–shell is not observed. To produce voids, the shell crystal must be in an intermediate sweet spot of size relative to the core particle.

In summary, tentative design rules have been formulated to synthesized yolk–shell particles without need for the sacrificial template commonly used to this end. First, the strategy of initial polymer adsorption sets the stage to allow shells of polycrystalline coordination polymer to grow regardless of the chemical makeup of the parent core particle that is underneath. Second, we find it is essential to have a moderate nucleation density followed by slow crystal growth to generate continuous shell. This can be achieved by fine-tuning the solvent polarity, precursor concentrations, and modulating ligands. A third design rule is that cavities form by shell deformation from anisotropic stress generated during the polycrystalline shell growth, in fashions predictable by considering the local curvature of the core particle.

ASSOCIATED CONTENT

Ⓢ Supporting Information

Complete descriptions of experimental procedures, characterization methods, and TEM images of the structures. This material is available free of charge via the Internet at http://pubs.acs.org.

AUTHOR INFORMATION

Corresponding Author
sgranick@illinois.edu
Notes
The authors declare no competing financial interest.

REFERENCES

(1) Kuo, C. H.; Tang, Y.; Chou, L. Y.; Sneed, B. T.; Brodsky, C. N.; Zhao, Z. P.; Tsung, C. K. *J. Am. Chem. Soc.* **2012**, *134*, 14345.
(2) Liu, Y.; Zhang, W.; Li, S.; Cui, C.; Wu, J.; Chen, H.; Huo, F. *Chem. Mater.* **2013**, *26*, 1119.
(3) Zhang, Z. C.; Chen, Y. F.; Xu, X. B.; Zhang, J. C.; Xiang, G. L.; He, W.; Wang, X. *Angew. Chem., Int. Ed.* **2014**, *53*, 429.
(4) Zhang, L.; Qiao, S. Z.; Jin, Y. G.; Chen, Z. G.; Gu, H. C.; Lu, G. Q. *Adv. Mater.* **2008**, *20*, 805.
(5) Zhu, Y. F.; Ikoma, T.; Hanagata, N.; Kaskel, S. *Small* **2010**, *6*, 471.
(6) Gao, J. H.; Liang, G. L.; Cheung, J. S.; Pan, Y.; Kuang, Y.; Zhao, F.; Zhang, B.; Zhang, X. X.; Wu, E. X.; Xu, B. *J. Am. Chem. Soc.* **2008**, *130*, 11828.
(7) Roca, M.; Haes, A. J. *J. Am. Chem. Soc.* **2008**, *130*, 14273.
(8) Fischer, R. A.; Woll, C. *Angew. Chem., Int. Ed.* **2009**, *48*, 6205.
(9) Koh, K.; Wong-Foy, A. G.; Matzger, A. J. *Chem. Commun.* **2009**, 6162.
(10) Lee, H. J.; Cho, Y. J.; Cho, W.; Oh, M. *ACS Nano* **2013**, *7*, 491.
(11) Lu, G.; Li, S. Z.; Guo, Z.; Farha, O. K.; Hauser, B. G.; Qi, X. Y.; Wang, Y.; Wang, X.; Han, S. Y.; Liu, X. G.; DuChene, J. S.; Zhang, H.; Zhang, Q. C.; Chen, X. D.; Ma, J.; Loo, S. C. J.; Wei, W. D.; Yang, Y. H.; Hupp, J. T.; Huo, F. W. *Nat. Chem.* **2012**, *4*, 310.
(12) Khaletskaya, K.; Reboul, J.; Meilikhov, M.; Nakahama, M.; Diring, S.; Tsujimoto, M.; Isoda, S.; Kim, F.; Kamei, K. I.; Fischer, R. A.; Kitagawa, S.; Furukawa, S. *J. Am. Chem. Soc.* **2013**, *135*, 10998.
(13) He, L. C.; Liu, Y.; Liu, J. Z.; Xiong, Y. S.; Zheng, J. Z.; Liu, Y. L.; Tang, Z. Y. *Angew. Chem., Int. Ed.* **2013**, *52*, 3741.
(14) Zhao, M. T.; Deng, K.; He, L. C.; Liu, Y.; Li, G. D.; Zhao, H. J.; Tang, Z. Y. *J. Am. Chem. Soc.* **2014**, *136*, 1738.
(15) Zhang, T. R.; Ge, J. P.; Hu, Y. X.; Zhang, Q.; Aloni, S.; Yin, Y. D. *Angew. Chem., Int. Ed.* **2008**, *47*, 5806.
(16) Huo, J.; Wang, L.; Irran, E.; Yu, H. J.; Ma, L.; Gao, J. M.; Fan, D. S.; Ding, W. B.; Amin, A. M.; Tai, Y. L. *J. Colloid Interface Sci.* **2012**, *367*, 92.
(17) Huo, J.; Wang, L.; Irran, E.; Yu, H. J.; Gao, J. M.; Fan, D. S.; Li, B.; Wang, J. J.; Ding, W. B.; Amin, A. M.; Li, C.; Ma, L. A. *Angew. Chem., Int. Ed.* **2010**, *49*, 9237.
(18) Sindoro, M.; Yanai, N.; Jee, A. Y.; Granick, S. *Acc. Chem. Res.* **2014**, *47*, 459.
(19) Venna, S. R.; Jasinski, J. B.; Carreon, M. A. *J. Am. Chem. Soc.* **2010**, *132*, 18030.
(20) Huang, X. C.; Lin, Y. Y.; Zhang, J. P.; Chen, X. M. *Angew. Chem., Int. Ed.* **2006**, *45*, 1557.
(21) Lamer, V. K.; Dinegar, R. H. *J. Am. Chem. Soc.* **1950**, *72*, 4847.